Neurobiology of Disease

Mechanisms and Consequences of Cerebellar Purkinje Cell Disinhibition in a Mouse Model of Duchenne Muscular Dystrophy

Wan-Chen Wu,[1] Samual P. Bradley,[2] Jason M. Christie,[2] and Jason R. Pugh[1,3]

[1]Department of Cellular and Integrative Physiology, University of Texas Health Science Center at San Antonio, San Antonio, Texas 78229, [2]Department of Physiology and Biophysics, University of Colorado School of Medicine, Aurora, Colorado 80045, and [3]Center for Biomedical Neuroscience, University of Texas Health Science Center at San Antonio, San Antonio, Texas 78229

Duchenne muscular dystrophy (DMD), the most common form of childhood muscular dystrophy, is caused by mutations in the dystrophin gene. In addition to debilitating muscle degeneration, patients display a range of cognitive deficits thought to result from the loss of dystrophin normally expressed in the brain. While the function of dystrophin in muscle tissue is well characterized, its role in the brain is still poorly understood. The highest expression of dystrophin in the mouse brain is in cerebellar Purkinje cells (PCs), where it colocalizes with $GABA_A$ receptor clusters. Using *ex vivo* electrophysiological recordings from connected molecular layer interneuron (MLI)–PC pairs, we investigated changes in inhibitory synaptic transmission caused by dystrophin deficiency. In male *mdx* mice (which lack long-form dystrophin), we found that responses at MLI–PC pairs were reduced by ~60% because of both decreased quantal response amplitude and a reduced number of functional vesicle release sites. Using electron microscopy, we found significantly fewer and smaller anatomically defined inhibitory synapses contacting the soma of PCs in *mdx* mice, suggesting that dystrophin may play a critical role in synapse formation and/or maintenance. Functionally, we found reduced MLI-evoked pauses in PC firing in acute slices. *In vivo* recordings from awake *mdx* mice showed increased sensory-evoked simple spike firing in positively modulating PCs, consistent with reduced feedforward inhibition, but no change in negatively modulating PCs. These data suggest that dystrophin deficiency in PCs disrupts inhibitory signaling in the cerebellar circuit and PC firing patterns, potentially contributing to cognitive and motor deficits observed in *mdx* mice and DMD patients.

Key words: **DMD; dystrophin; inhibition; *mdx*; Purkinje; synapse**

Significance Statement

Duchenne muscular dystrophy (DMD) is primarily characterized by progressive muscle weakening caused by genetic mutations in the gene for dystrophin. Dystrophin is also normally expressed in the CNS, and DMD patients experience a range of nonprogressive cognitive deficits. The pathophysiology of CNS neurons resulting from loss of dystrophin and the function of dystrophin in neurons are still poorly understood. Using cerebellar PCs as a model, we found that the loss of dystrophin specifically disrupts the number and strength of inhibitory synaptic connections, suggesting that dystrophin participates in formation and/or maintenance of these synapses. This work provides insight into the function of dystrophin in the CNS and establishes neuronal and synaptic dysfunction, which may underlie cognitive deficits in DMD.

Introduction

Duchenne muscular dystrophy (DMD), an X-linked disorder arising from mutations in the gene for dystrophin, is the most common form of muscular dystrophy affecting 1 in ~3000–5000 males at birth (Emery, 1991). This disorder is most commonly associated with progressive muscle degeneration and wasting; however, severe nonprogressive cognitive deficits have also been identified in DMD patients from the earliest descriptions of the disease (Duchenne, 1868). The most commonly reported deficits include intellectual disability (average full-scale IQ, ~80; Billard et al., 1992; Cotton et al., 2001, 2005; Ricotti et al., 2016),

Received June 18, 2021; revised Dec. 13, 2021; accepted Jan. 8, 2022.

Author contributions: W.-C.W., S.P.B., J.M.C., and J.R.P. designed research; W.-C.W. and S.P.B. performed research; W.-C.W., S.P.B., J.M.C., and J.R.P. analyzed data; J.R.P. wrote the paper.

This work was funded by National Institutes of Health Grants NS-092809, NS-123933, and NS-112289), and a Young Investigator Award from the Max and Minnie Tomerlin Voelcker Fund. We thank Andrew Ginsberg and Rebecca Howell for collecting preliminary room temperature data for this project. We also thank the Electron Microscopy Laboratory at University of Texas Health Science Center at San Antonio for support on electron microscopy studies.

The authors declare no competing financial interests.

Correspondence should be addressed to Jason R. Pugh at pughj@uthscsa.edu.

https://doi.org/10.1523/JNEUROSCI.1256-21.2022

impaired verbal expression (Karagan et al., 1980), and reduced working memory (Hinton et al., 2000). DMD patients also show high comorbidity with other neurodevelopmental conditions, such as autism spectrum disorder, attention-deficit/hyperactivity disorder, and obsessive-compulsive disorder (Wu et al., 2005; Pane et al., 2012; Fujino et al., 2018; Darmahkasih et al., 2020). These findings suggest that the dysfunction in DMD may extend beyond the muscular system to the CNS. In fact, full-length dystrophin expression has been observed in multiple regions of the CNS including hippocampus, cortex, amygdala, and cerebellum, with the highest expression in cerebellar Purkinje cells (PCs; Geng et al., 1991; Lidov et al., 1993). However, the role of dystrophin in neuronal function remains unclear.

Dystrophin is a member of the dystroglycan complex (DGC), a large complex of proteins that span the cellular membrane. In muscle cells, the DGC forms a link between the intracellular cytoskeleton (through dystrophin, which binds both actin and DGC proteins) and the extracellular matrix (through α-dystroglycan; Gao and McNally, 2015). In neurons, dystrophin expression is also associated with the DGC and dystrophin labeling colocalizes with $GABA_A$ receptor ($GABA_AR$) clusters and markers of inhibitory postsynaptic densities (Knuesel et al., 1999; Briatore et al., 2020). In *mdx* mice, the most widely used model of DMD, which lack full-length dystrophin expression, $GABA_AR$ clustering (Knuesel et al., 1999; Grady et al., 2006) and miniature IPSC (mIPSC) amplitudes (Anderson et al., 2003; Kueh et al., 2008) are reduced in PCs, suggesting that dystrophin and the DGC play a role in postsynaptic receptor clustering. However, the number of $GABA_AR$ clusters (Grady et al., 2006) and the frequency of mIPSCs (Kueh et al., 2008) are also reduced in *mdx* PCs, possibly indicating fewer inhibitory synapses contacting each PC. This raises the possibility that the DGC plays a role in synapse formation in PCs, possibly participating in transsynaptic cell adhesion (Briatore et al., 2020).

Cerebellar dysfunction has been hypothesized to contribute to DMD phenotypes (Cyrulnik and Hinton, 2008); however, the physiological consequences of the loss of dystrophin in PCs are still poorly understood. Previous studies in PCs have focused on immunolabeling of dystrophin and associated proteins or analysis of spontaneous IPSCs. To understand how the loss of dystrophin alters inhibitory synaptic transmission and firing in PCs, we made simultaneous electrophysiological recordings from synaptically connected pairs of molecular layer interneurons (MLIs) and PCs from control and *mdx* mice. We found a significant reduction in inhibitory, but not excitatory, synaptic input to PCs in *mdx* mice. Reduced inhibitory input was caused by both smaller quantal amplitude and a reduced number of functional release sites, with no change in vesicular release probability (Pr) or replenishment rate. Using electron microscopy (EM), we also found that the number of anatomically defined inhibitory synapses contacting each PC soma was reduced in *mdx* tissue. Together, these data support the view that dystrophin and the DGC play a role in the formation and/or maintenance of inhibitory synapses. In acute slices, loss of dystrophin increased the regularity of PC firing and reduced pauses in PCs evoked by the stimulation of a connected MLI. In awake *mdx* mice, sensory-evoked responses in positively modulating PCs showed greater levels of firing. These data provide the most complete physiological investigation of changes in PC synaptic and firing behavior resulting from loss of dystrophin to date.

Materials and Methods

Animals. All procedures involving animals were approved in advance by the Institutional Animal Care and Use Committee of the University of Texas Health Science Center at San Antonio or the University of Colorado Anschutz Medical Campus. For all acute brain slice experiments, male *mdx* mice (C57BL/10ScSn-Dmd^{mdx}/J; catalog #001801, The Jackson Laboratory) and wild-type (WT) littermate controls aged postnatal day 14 (P14) to P21 or P44 to P46 were used. For *in vivo* recordings, male *mdx* and C57BL/10ScSnJ (catalog #000476, The Jackson Laboratory) control mice were used (P42 to P70). Male mice were used to better model DMD, an X-linked disorder that primarily affects human males. Mice were age matched across genotype for all experiments (difference in average age < 1.5 d). *mdx* mice begin to show muscle deficits beginning at P14, but because of muscle regeneration and adaptation, motor phenotypes are observed only during a brief period in late development (2–5 weeks of age) and beyond 6 months of age (Muntoni et al., 1993; Massopust et al., 2020). Animals were housed with a dam and maintained on a standard 12 h light/dark cycle with *ad libitum* access to water and food.

Slice preparation. Acute parasagittal brain slices were prepared from male WT and *mdx* mice each day. Mice were anesthetized by isoflurane inhalation and cerebellar tissue was immediately extracted and placed in ice-cold artificial CSF (ACSF) containing the following (in mM): 119 NaCl, 26.2 $NaHCO_3$, 2.5 KCl, 1 NaH_2PO_4, 11 glucose, 2 $CaCl_2$, and 1.3 $MgCl_2$. Acute parasagittal slices (300 μm) of the vermis were cut using a vibratome (model VT1200S, Leica Biosystems) and incubated at 34°C for 30 min in oxygenated ACSF. Following recovery, slices were maintained at room temperature until being transferred to a recording chamber.

Slice electrophysiology. All experiments were performed at 31.5–33°C, except where noted. During recording, slices were superfused with ACSF at a flow rate of ~2 ml/min in the recording chamber. Spontaneous EPSCs (sEPSCs) were isolated pharmacologically by including 100 μM picrotoxin (PTX; Abcam Biochemicals) and 100 μM cyclothiazide (Toronto Research Chemicals) in bath ACSF to block $GABA_ARs$ and to enhance AMPA-mediated currents, respectively. To avoid potentially confounding effects of bath PTX or cyclothiazide, we also recorded sEPSCs in the absence of pharmacological agents and isolated sEPSCs by recording at or near the chloride equilibrium potential (approximately −70 mV). For IPSC recordings, 10 μM R-CPP (Sigma-Aldrich) and 10 μM NBQX (Toronto Research Chemicals) were added to the bath solution to block fast excitatory synaptic currents. In a subset of experiments, sIPSC were recorded in the absence of NBQX or CPP. In these experiments, sIPSCs were isolated by holding the PC membrane potential at 0 mV. In experiments measuring mIPSCs, 100 or 500 nM tetrodotoxin (TTX; Sigma-Aldrich) was included in the bath solution to block sodium channel-dependent action potentials (APs; in recordings from MLIs, we confirmed that 100 nM TTX was sufficient to abolish evoked APs). Whole-cell patch-clamp recordings were made from PCs using pipettes pulled from borosilicate glass capillaries (tip resistance, 2–4 MΩ; Sutter Instruments). For EPSC and AP recordings, pipettes were filled with a K-gluconate-based internal solution containing the following (in mM): 137 K-gluconate, 10 HEPES, 5 EGTA, 4 $MgCl_2$, 2 KCl, 4 Na-ATP, and 0.5 Na-GTP. When measuring IPSCs, pipettes were filled with a high chloride internal solution containing the following (in mM): 135 CsCl, 10 HEPES, 5 EGTA, 4 Na-ATP, 0.5 Na-GTP, and 2 QX-314. For sIPSC recordings in the absence of NBQX or CPP, pipettes were filled with an internal solution containing the following (in mM): 130 Cs-gluconate, 10 HEPES, 5 EGTA, 1 NaCl, 1 $MgCl_2$, 1 $CaCl_2$, and 3 Mg-ATP. MLIs were patched using 4–6 MΩ borosilicate pipettes filled with an internal solution containing the following (in mM): 134 K-gluconate, 10 HEPES, 4 $MgCl_2$, 4 Na-ATP, 0.5 Na-GTP, 10 GABA, and 50 μM Alexa Fluor 594. For all internal solutions, the pH was adjusted to 7.2–7.4, and the osmolarity ranged from 280 to 300 mOsm. Electrophysiological recordings were acquired and filtered at 10 kHz with a MultiClamp 700B amplifier (Molecular Devices) and digitized at 20 kHz with a Digidata 1550B digitizer (Molecular Devices).

To perform recordings from synaptically connected MLI–PC pairs, cells in the inner third of the molecular layer were first patched and filled with Alexa Fluor 594. We increased the likelihood of finding connected MLI–PC pairs using epifluorescence to visually identify the MLI axon and target PCs in the vicinity of the labeled axon for patching. To test for synaptic connectivity in each MLI–PC pair, a 100 Hz train of APs (400 ms) was evoked in the MLI by brief depolarizing current injections, and the presence of time-locked IPSCs in the postsynaptic PC was determined by visual inspection of individual and averaged traces. PCs in which MLI firing did not evoke an identifiable IPSC were not used for further data collection. In paired recording experiments measuring IPSCs, MLIs were held in current-clamp mode and PCs were held at −60 mV in voltage-clamp mode. To measure recovery from vesicle depletion, we evoked a 100 Hz train (40 APs) in the MLI to deplete the readily releasable pool (RRP) of vesicles. Steady-state depression was not different between genotypes ($p = 0.79$), suggesting that depletion of the RRP was similar across both groups. The time course of IPSC recovery was measured by evoking single MLI APs over a range of intervals following the train and recorded the corresponding IPSC amplitudes. Recovery fractions for each time point were determined by normalizing the IPSC amplitude to the amplitude of the first IPSC in the 100 Hz train (IPSCn/IPSC1). The recovery rate (tau) for each genotype was derived by fitting a single exponential function to a plot of the recovery fractions. AP waveform analysis was performed on PC APs from step current injection experiment. The parameters from the analysis were acquired running an in-house script on Igor Pro software (version 6; WaveMetrics). For each cell, the first AP was analyzed from the minimum AP-inducing current injection and averaged across three separate sweeps. In paired experiments examining MLI control of PC firing, whole-cell recordings were made from MLIs in current-clamp mode, and cell-attached recordings were made from PCs. In this case, we tested for connectivity by stimulating a 50 Hz train of APs in the MLI; only PCs that showed at least a 5% reduction in firing during the MLI stimulation were considered connected. Using these criteria, it is possible we missed very weakly connected pairs. However, this is likely to result in an underestimate in the difference between WT and *mdx*, as we were more likely to miss weakly connected *mdx* pairs.

Cumulative IPSC analysis. Cumulative IPSC analysis was used to estimate the size of the RRP and the release probability at MLI–PC synapses. After establishing a paired recording from connected MLIs and PCs, trains of 40 APs at 100 Hz were evoked in the presynaptic MLI by depolarizing current injections, and IPSCs were recorded in the PC. For each pair, we used analysis of cumulative IPSCs (average, 20 sweeps) to estimate RRP and release probability (Schneggenburger et al., 1999; Thanawala and Regehr, 2013). In this analysis ("train method"), the cumulative IPSC was plotted against stimulus number and a linear function was fit to the last 15 points. The *y*-intercept extrapolated from this linear fit represents the total postsynaptic current expected from the release of the RRP in the absence of vesicle replenishment. RRP size for each pair was determined by dividing the *y*-intercept of the linear fit by the average mIPSC amplitude measured in WT or *mdx* PCs. The release probability was estimated for each pair by dividing the extrapolated *y*-intercept by the amplitude of the first IPSC. We also used a second independent method to measure RRP and release probability, first described by Elmqvist and Quastel (1965). This second method ("EQ method") is reliable across a wider range of release probabilities and stimulus frequencies, particularly at synapses that do not show facilitation, as was the case at MLI–PC synapses (Thanawala and Regehr, 2013). In this analysis, each IPSC amplitude was plotted against the cumulative IPSC amplitude, and a linear fit was made to the first five points. The extrapolated *x*-intercept from this fit was divided by the average mIPSC amplitude for each genotype to obtain the RRP size. The release probability was calculated by dividing the *x*-intercept of the linear fit by the amplitude of the first IPSC.

Quantal analysis. To measure parameters of synaptic transmission, we applied quantal analysis to recordings of IPSCs from connected MLI–PC pairs. A subset of MLI–PC pairs from each genotype used for quantal analysis were recorded at room temperature. We did not find differences in quantal parameters across recording temperatures, so data from both temperatures were combined for analysis. For each pair, we created a frequency histogram of individual IPSC amplitudes. Histograms showed a regular pattern of peaks and valleys that were clearly identifiable by eye, consistent with quantal release of neurotransmitter (Boyd and Martin, 1956; Martin, 1966). The identification of peaks was confirmed by fitting each histogram using the sum of Gaussian functions of the following form:

$$\text{Summed Gaussian function} : \sum A e^{-\left\{\frac{x-(p*s)}{w}\right\}^2},$$

where A is the amplitude of each Gaussian (determined by a Poisson function, see below), p is the number of the peak, s is the period of the peaks, and w is the width of the Gaussians (Boyd and Martin, 1956; Edwards et al., 1990). The number of summed Gaussian functions used for each fit was determined by the number of peaks in the frequency histogram. The average quantal amplitude for each MLI–PC pair was determined by the position of the first peak of the histogram above zero and by the period of the Gaussian fit (s in the above equation).

The peaks of each histogram were fit with Poisson and binomial functions (Castellucci and Kandel, 1974) of the following form:

$$\text{Poisson function} : A e^{-m}\left(\frac{m^x}{x!}\right)$$

$$\text{Binomial function} : A\left(\frac{n!}{x!(n-x)!}\right)\cdot p^x \cdot (1-p)^{(n-x)},$$

where x is the peak number, A is the amplitude, m is the mean quantal content, n is the number of release sites, and p is the release probability. The average quantal content of IPSCs and the number of release sites for each MLI–PC pair were determined by the m and n values derived from the Poisson or binomial fit of each IPSC frequency histogram. These values were then averaged across all MLI–PC pairs for each genotype.

Transmission electron microscopy. In preparation for transmission EM, P16–P19 WT and *mdx* mice were transcardially perfused with 0.1 M PBS and 4% glutaraldehyde. Brains were extracted and fixed overnight in the same solution. Cerebellar samples were submitted to University of Texas Health Science Center at San Antonio Electron Microscopy Laboratory where 90 nm sections were cut and mounted on copper grids. Images were acquired using a microscope (model 1400, JEOL). PC somata were first identified in 4000× magnified images. To identify synaptic contacts, high-resolution images (50,000×) were acquired of the entire circumference for each PC soma. Putative inhibitory synapses were identified by axon terminals in direct contact with the PC soma containing the following: (1) at least one mitochondria; (2) at least one active zone (AZ; darkening of presynaptic plasma membrane) including a cluster of clearly visible synaptic vesicles; and (3) a corresponding darkening of postsynaptic plasma membrane opposite the AZ representing the postsynaptic density (indicating a GABAergic synapse). PC terminals were clearly identifiable by the presence of numerous synaptic vesicles and darkening of the axoplasm (Palay and Chan-Palay, 1974; Briatore et al., 2020; Ichikawa et al., 2011). Parallel fibers were frequently observed in the outer third of the soma, but were easily identified by small, nearly round boutons and asymmetrical synapses (Palay and Chan-Palay, 1974). Inhibitory synapses (those containing a clear postsynaptic density) that were not PC terminals and contacting a PC soma were presumed to be MLI synapses. However, we cannot rule out the possibility that a small number of these synapses arose from other cell types. AZ length was measured in ImageJ software (https://imagej.nih.gov/ij/) using a freehand line extending the total distance where presynaptic and postsynaptic darkening was evident. In cases where two or three separate densities were observed in the same presynaptic terminal, each synaptic density was counted as a single synapse when clearly separated. However, it is possible that these represent a single synaptic density, given the often complex three-dimensional morphology of synaptic densities. Synaptic vesicles were counted by eye. Docked and clustered vesicles were defined as those within 10 and 200 nm of the AZ, respectively. The experimenter was blinded to genotype during quantitative analysis of EM images.

Surgical procedures for in vivo *PC recording.* Mice were prepared for *in vivo* electrophysiological recording using surgical procedures performed under continuous isoflurane (1–2%) anesthesia. Mice were placed in a stereotactic frame (model 940, Kopf Instruments) incorporating a heating pad with biofeedback from a rectally inserted thermometer. For pain control, buprenorphine (1.0 mg/ml) was administered by subcutaneous injection, as well as local application of lidocaine/bupivacaine (1.0 mg/ml, 0.2 mg/ml) under the scalp; dexamethasone (0.6 mg/ml; subcutaneous injection) was used to limit inflammation. After removal of a portion of the scalp, a stainless steel head-post was cemented (Metabond, Parkell) to the exposed skull. A small craniotomy (2.35 mm drill bit) was made over left lobules Crus I/II (2.5–3.3 mm lateral to bregma; 5.8–6.3 mm caudal to bregma) and filled with elastomer (Kwikcast, World Precision Instruments). Additionally, a small craniotomy was made on the anterior portion of the skull and a silver reference wire was cemented in place. Any remaining exposed skull was covered with dental cement.

In vivo *recording.* Following surgery, the mice were allowed to recover for >1 h before the first electrophysiological recording session; experimental sessions continued up to 4 d postsurgery. Briefly, mice were restrained using the implanted head-post on a purpose-built apparatus that was placed in a light-proof and sound-dampened enclosure. The elastomer was removed from the craniotomy, and saline was applied to the exposed brain. A high-electrode density silicon probe (catalog #H6b, Cambridge Neurotech) was inserted into the cerebellar cortex using a micromanipulator (Kopf Instruments). The depth of insertion was determined by the level of unit activity observed across all channels of the probe. The probes were connected to an amplifier (model RHD2132, Intan Technologies), and neural activity was collected using commercial software (Intan Technologies) at a sampling rate of 20 kHz. Following a 2 min period of quiescence (i.e., quiet wakefulness), the mice were exposed to an unexpected blue light flash (473 nm, 25 mW) from an LED placed adjacent to the left eye or to an audible tone (10 kHz, 90 dB) from a speaker placed adjacent to the left ear. The light or tone was presented in blocks of 15 trials of the same stimulus modality, with each stimulus lasting 250 ms and a pseudorandom interstimulus interval of 1.5–2 s. Timing was controlled using a commercial system (Bpod, Sanworks).

In vivo *electrophysiology analysis.* The data from the multiunit recordings were sorted using the Kilosort algorithm (version 2.5; Pachitariu et al., 2016) and manually curated using Phy2 software (https://github.com/cortex-lab/phy). Unambiguous PC units were first identified based on the presence of stereotypical complex spikes, as determined by a pause in simple spike firing in the cross-correlation between the isolated simple spiking unit and subsequent complex spike unit ($n = 18$). We further used spike rates (>40 Hz) and a large spatial distribution of electrical activity across the probe electrodes (more than six separate channels) to identify additional putative PCs ($n = 29$; Gaffield and Christie, 2021).

Simple spike activity from the curated PC units was binarized for further analysis. Mean firing rates during quiescence were calculated over a 2 min recording period. Firing regularity was determined by calculating the coefficient of variation (CV) of the interspike interval (ISI). To assess mean firing rates during sensory stimuli, the simple spikes were aligned to stimulus onset and binned (25 ms intervals). Peristimulus time histograms were constructed for each cell, and the mean firing was calculated during the sensory stimulation period (250 ms). PCs showing a >5% increase or decrease in firing during the sensory stimuli, relative to baseline, were classified as positively or negatively modulating, respectively. The effect of genotype on mean and peak firing rate were analyzed separately between these two groupings. The change in mean firing rate was computed relative to the prestimulus mean firing rate. For peak firing rate, the simple spiking responses were rebinned (5 ms intervals) and either the peak increase or decrease in activity was determined during stimulus presentation for either positively or negatively modulating PCs, respectively. Notably, there was one outlier PC from the negatively modulating *mdx* group, which we removed from our analysis because it did not change the significance of any comparison test.

Experimental design and statistical analyses. For all datasets, experimental values are compared between WT and *mdx*. Data are presented as the mean ± SEM, and *n*-values represent the number of cells recorded. Statistical comparisons were achieved using Prism (version 6; GraphPad) and Igor Pro (version 6; WaveMetrics). Unpaired two-tailed Student's *t* tests (normally distributed datasets), Mann–Whitney tests (skewed datasets), or two-way repeated-measures ANOVA were used to determine statistical significance. Statistical differences with $p < 0.05$ were considered significant: $^{*}p < 0.05$, $^{**}p < 0.01$, $^{***}p < 0.001$, and $^{****}p < 0.0001$.

Results

Inhibitory synaptic transmission is reduced in *mdx* PCs

To investigate how the loss of dystrophin affects synaptic function in PCs, we first recorded pharmacologically isolated spontaneous excitatory and inhibitory synaptic events in PCs using whole-cell patch-clamp recordings in acute cerebellar slices from WT and *mdx* mice. We did not find a difference in sEPSC amplitude (WT: 26.4 ± 0.7 pA, $n = 13$; *mdx*: 27.4 ± 1.6 pA, $n = 9$; $p = 0.52$) or frequency (WT: 3.2 ± 0.3 Hz; *mdx*: 3.0 ± 0.6 Hz; $p = 0.83$; Fig. 1*A*,*B*) between genotypes. This suggests that parallel fiber synaptic transmission is not altered in *mdx* mice (sEPSCs are primarily mediated by parallel fiber synapses in PCs; Takahashi and Linden, 2000). Because PTX may alter parallel fiber transmission through the inhibition of presynaptic $GABA_A$Rs (Stell et al., 2007; Pugh and Jahr, 2011; Khatri et al., 2019), we also recorded sEPSCs in the absence of pharmacological agents. With cells held near the Cl^- equilibrium potential to isolate excitatory synaptic events, we again did not observe a difference in sEPSC amplitude ($p = 0.48$) or frequency ($p = 0.58$) across genotypes. By contrast, we found that pharmacologically isolated sIPSCs were significantly reduced in amplitude (WT: 80.5 ± 5.5 pA, $n = 10$; *mdx*: 57.4 ± 2.9 pA, $n = 14$; $p = 0.0006$) and frequency (WT: 14.4 ± 1.7 Hz; *mdx*: 2.7 ± 0.4 Hz; $p < 0.0001$; Fig. 1*C*,*D*) in *mdx* PCs. This was also true when IPSCs were isolated by holding the cell at 0 mV, in the absence of NBQX or CPP (amplitude: 119.2 ± 12.7 vs 58.6 ± 3.7 pA, $p = 0.001$; frequency: 19.7 ± 1.2 vs 14.5 ± 0.9 Hz, $n = 7$–9, $p = 0.007$). Evoked AP firing in MLIs was not different across genotype (two-way repeated-measures ANOVA, $F_{(1,7)} = 0.95$; main effect $p = 0.36$), suggesting that the differences in sIPSCs are not because of a change in MLI excitability (data not shown). Further, mIPSC (recorded in the presence of TTX) amplitude (WT: 31.8 ± 1.8 pA, $n = 18$; *mdx*: 23.8 ± 1.2 pA, $n = 18$; $p = 0.0008$) and frequency (WT: 6.0 ± 0.6 Hz; *mdx*: 2.4 ± 0.3 Hz; $p < 0.0001$; Fig. 1*E*,*F*) were also reduced in *mdx* PCs. To test whether deficits in IPSCs persist beyond development, we also recorded mIPSCs from 6- to 7-week-old mice. In older mice, we again found that mIPSC amplitude (WT: 51.2 ± 2.3 pA, $n = 10$; *mdx*: 39.9 ± 1.4 pA, $n = 5$; $p = 0.007$) and frequency (WT: 3.7 ± 0.6 Hz; *mdx*: 1.4 ± 0.1 Hz; $p = 0.01$; Fig. 1*G*,*H*) were reduced, suggesting that deficits in inhibitory synaptic transmission are not related to developmental delay of synapse formation in *mdx* mice. Overall, these experiments revealed that loss of dystrophin selectively impairs inhibitory synaptic transmission in PCs with no effect observed on spontaneous excitatory synaptic transmission. The reduction in sIPSC and mIPSC amplitudes is likely explained by reduced postsynaptic $GABA_A$R clustering, as has been previously suggested (Knuesel et al., 1999; Kueh et al., 2011). However, reduced mIPSC frequency could be caused by several factors, including reduced vesicle release probability, reduced number of inhibitory synapses, or undercounting of IPSCs in *mdx* PCs from loss of smaller-amplitude events in the background noise.

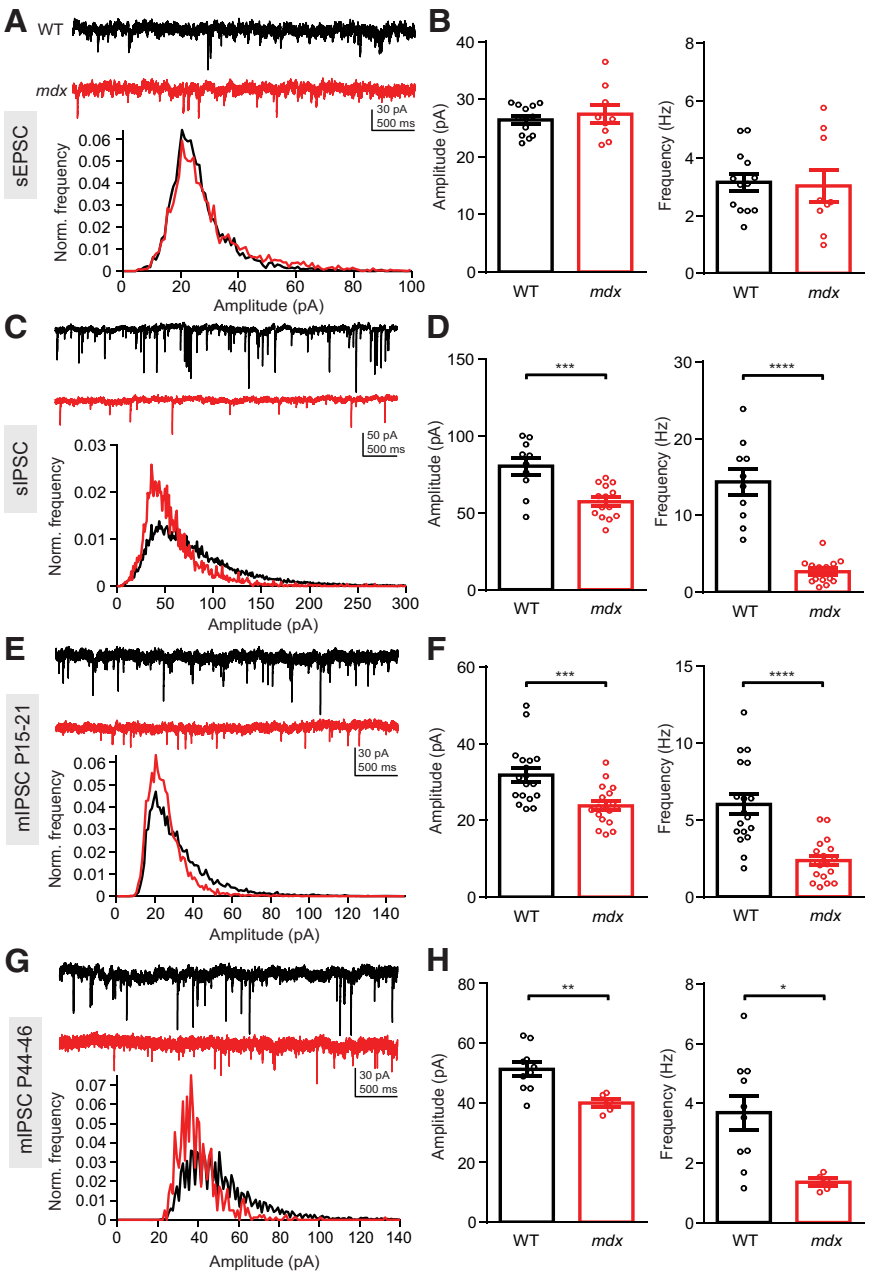

Figure 1. Inhibitory synaptic currents are impaired in *mdx* PCs. ***A***, Top, Representative sEPSC traces from a WT (black) and *mdx* (red) PC. Bottom, Normalized event distribution plot showing all sEPSC events recorded from WT and *mdx* PCs. ***B***, Average sEPSC amplitude (left) and frequency (right) in WT and *mdx* PCs. ***C***, Top, Representative sIPSC traces from a WT (black) and *mdx* (red) PC. Bottom, Normalized sIPSC distribution plots. ***D***, Average sIPSC amplitude (left) and frequency (right) in WT and *mdx* PCs. ***E***, Top, Representative mIPSC traces from a WT (black) and *mdx* (red) PC from P15 to P21 mice. Bottom, Normalized mIPSC distribution plots. ***F***, Average mIPSC amplitude (left) and frequency (right) in P15 to P21 WT and *mdx* PCs. ***G***, Top, Representative mIPSC traces from a WT (black) and *mdx* (red) PC from P44 to P46 mice. Bottom, Normalized mIPSC distribution plots. ***H***, Average mIPSC amplitude (left) and frequency (right) in P44 to P46 WT and *mdx* PCs. Circles in bar graphs represent individual data points. * $p < 0.05$, ** $p < 0.01$, *** $p < 0.001$ and **** $p < 0.0001$.

To distinguish between these possibilities and to characterize differences in inhibitory synaptic properties in WT and *mdx* PCs more fully, we made simultaneous recordings from pairs of synaptically connected MLIs and PCs (Fig. 2*A*). In these experiments, single or pairs of APs were evoked by brief (5 ms) current injection through the patch pipette in the presynaptic MLI, and the resulting IPSCs were recorded in the postsynaptic PC. In paired recordings, there was no difference in evoked IPSC (eIPSC) rise time ($p = 0.59$) or decay kinetics ($p = 0.41$). However, there was a significant increase in the IPSC latency in *mdx* PCs (WT: 0.22 ± 0.05 ms, $n = 7$; *mdx*: 0.47 ± 0.08, $n = 7$; $p = 0.02$), possibly reflecting a change in calcium channel position/function or vesicle docking (Sabatini and Regehr, 1999). The average eIPSC amplitude was reduced by ~60% in *mdx* PCs (WT: 212.8 ± 25.2 pA, $n = 9$; *mdx*: 86.8 ± 29.6 pA, $n = 14$; $p = 0.007$; Fig. 2*B*), a much larger reduction than we found for sIPSC or mIPSC amplitudes. This larger reduction in amplitude is likely the result of a higher synaptic failure rate (defined as the percentage of sweeps in which an AP was evoked in the MLI, but no IPSC was evident in the connected PC on the first AP; Fig. 2*C*) in *mdx* cells. IPSC failures were almost nonexistent in WT cells (1.0 ± 1.0% of sweeps, $n = 10$) but were common in *mdx* PCs (34.6 ± 9.2% of sweeps, $n = 14$, $p = 0.006$; Fig. 2*D*). In some recordings from *mdx* PCs, IPSCs were very rarely observed following the first MLI AP, although connectivity between the two neurons was evident by the presence of time-locked IPSCs following the second AP. This explains why the average eIPSC amplitudes in some *mdx* MLI–PC pairs are at or very near zero (Fig. 2*B*). The failure rate can be increased by at least two likely mechanisms: a reduction in vesicle release probability or a decrease in the number of synapses activated (in this case, the number of synaptic contacts between a single MLI and a single PC).

To distinguish between these two possible mechanisms, we measured vesicle release probability at MLI synapses in each genotype by two methods. First, we measured the paired-pulse ratio (PPR) over a range of interstimulus intervals in connected MLI–PC pairs. We did not find a difference in PPR between WT and *mdx* cells (two-way repeated-measures ANOVA, $F_{(1,15)} = 0.175$; main effect, $p = 0.68$; Fig. 3*A*), suggesting that release probability does not differ across genotypes. In a second set of experiments, we evoked trains of APs (40 stimuli at 100 Hz) in MLIs and recorded the corresponding IPSCs from connected PCs (Fig. 3*B*). From these data, we used two independent methods to estimate release probability and the size of the RRP: the train method (Schneggenburger et al., 1999; Fig. 3*D*) and the EQ method (Elmqvist and Quastel,1965; Fig. 3*F*; see Materials and Methods). The train method overestimates release probability and underestimates the RRP, and the EQ method underestimates release probability and overestimates the RRP. Using both methods, we were able to establish lower and upper bounds for each value (Thanawala and Regehr, 2013). Using

either method, we did not find a difference in release probability at MLI synapses across genotypes (Pr_{Train}: WT: 0.17 ± 0.01, $n = 7$; *mdx*: 0.21 ± 0.03, $n = 7$, $p = 0.17$; Pr_{EQ}: WT: 0.10 ± 0.01; *mdx*: 0.14 ± 0.01, $p = 0.24$; Fig. 3*E*,*G*). Together, our PPR and cumulative IPSC data indicate that there is no change in vesicle release probability at MLI synapses between genotypes. We also did not find a difference in the recovery of eIPSC amplitude following high-frequency stimulation between genotypes ($n = 7$–9; two-way repeated-measures ANOVA, $F_{(1,14)} = 3.033$; main effect, $p = 0.1$; Fig. 3*H*,*I*), suggesting that altered replenishment of releasable vesicles does not account for the differences in eIPSC amplitude or failure rate. This raises the possibility that reduced mIPSC frequency and increased failure rate in *mdx* PCs is, instead, the result of a reduced number of inhibitory synaptic contacts between MLIs and PCs. Consistent with this possibility, we found that the RRP size (estimated from cumulative IPSC plots) in *mdx* MLI–PC pairs was significantly smaller compared with WT pairs using either the train method (RRP_{Train}: WT: 47.4 ± 4.5 vesicles, $n = 7$; *mdx*: 13.5 ± 1.3 vesicles, $n = 7$; $p = 0.017$; Fig. 3*E*) or the EQ method (RRP_{EQ}: WT: 73.2 ± 7.9 vesicles; *mdx*: 21.0 ± 1.4 vesicles; $p = 0.029$; Fig. 3*G*). To approximately estimate the quantal content for each pair, we divided the average eIPSC amplitude (Fig. 2*B*) by the mIPSC amplitude (Fig. 1*F*) for each genotype, giving the number of vesicles released on average following a single presynaptic AP. We found an ~50% decrease in the average number of vesicles released in *mdx* pairs (WT: 6.7 ± 0.8, $n = 9$; *mdx*: 3.6 ± 1.2, $n = 14$; $p = 0.085$; Fig. 3*J*), though this difference did not reach significance. Given the lack of change in release probability, this difference raises the possibility that MLIs form fewer synaptic contacts with PCs in *mdx* mice.

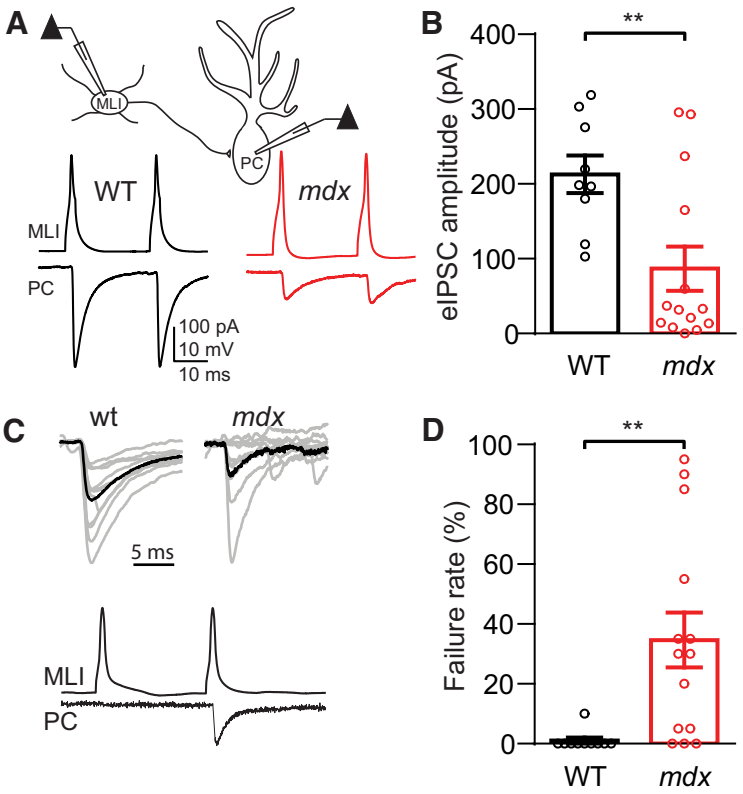

Figure 2. Evoked IPSCs are reduced in MLI–PC paired recordings. ***A***, Top, Simplified diagram of simultaneous MLI–PC paired recording. Bottom, Representative traces of MLI APs and resulting eIPSCs in connected PCs from a WT (black) and *mdx* (red) animal. ***B***, Average eIPSC amplitude in WT and *mdx* PCs. ***C***, Top, Ten consecutive eIPSC traces (gray) and average eIPSC trace (black) from WT and *mdx* PCs, showing synaptic failures in *mdx*. Bottom, Traces from a connected MLI–PC pair showing a synaptic failure following the first AP. ***D***, Average synaptic failure rate in WT and *mdx* PCs. Circles in bar graphs represent individual data points. ** $p < 0.01$.

Inhibitory synapse number is reduced in *mdx* PCs

To more accurately measure the number of release sites between a single MLI–PC pair, we applied quantal analysis to recordings of PC eIPSCs. When individual eIPSC traces from an MLI–PC pair were plotted together, we observed that eIPSC amplitudes frequently increased in a step-like fashion (Fig. 4*A*), suggesting that each step-up in amplitude represents the release of an additional vesicle. Frequency histograms of eIPSC amplitudes for each MLI–PC pair also showed regular peaks and valleys that were well fit by a sum of Gaussian equations (see Materials and Methods), consistent with quantal increases in eIPSC amplitudes (Martin, 1966; Fig. 4*B*,*C*). From these plots, we first estimated the quantal amplitude using two independent methods, the location of the first peak above zero (generally representing IPSCs resulting from release of a single vesicle; Fig. 4*C*) and the period of the fitting function (distance between peaks). Importantly, both estimates of quantal size matched closely across MLI–PC pairs (Fig. 4*D*). In a few pairs (mainly WT), the value of the first peak was an integer multiple of the period, suggesting that a single vesicle was never released in these pairs and the first peak of the histogram represents eIPSCs resulting from two or three vesicles (e.g., the pair in Fig. 4*B*). We found that the quantal size is reduced in *mdx* pairs when estimated by the amplitude of the first histogram peak (WT: 74.7 ± 16.2 pA, $n = 16$; *mdx*: 31.5 ± 6.9 pA, $n = 16$; $p = 0.02$) or by the period (WT: 47.8 ± 7.1 pA, $n = 16$; *mdx*: 26.2 ± 6.5 pA, $n = 16$; $p = 0.03$; Fig. 4*E*), consistent with the reduced mIPSC amplitude. The eIPSC frequency histogram from WT pairs tended to have more peaks and little or no peak at 0 pA (representing failures), suggesting more functional release sites in WT pairs. This difference was quantified by fitting the peaks of each frequency histogram with Poisson and binomial functions. From these fits, we found reduced quantal content of eIPSCs (m; WT: 6.5 ± 0.8, $n = 16$; *mdx*: 3.2 ± 0.7, $n = 16$; $p = 0.005$; Fig. 4*F*) and reduced number of functional release sites (n; WT: 32.6 ± 3.2, $n = 16$; *mdx*: 16.2 ± 2.8, $n = 16$; $p = 0.0006$; Fig. 4*G*) in *mdx* pairs. These data are remarkably consistent with the changes in RRP size and the average number of vesicles released per AP that we observed in Figure 3, *E* and *J*. These data provide physiological evidence that the number of release sites between MLIs and PCs is reduced by about half in *mdx* mice, suggesting that inhibitory synapses are either not formed or not maintained in the cerebella of *mdx* mice.

Anatomically defined inhibitory synapses contacting the soma of WT and *mdx* PCs were also quantified using EM (Fig. 5*A*,*B*). By P15, synaptic contacts at the soma or axon hillock of

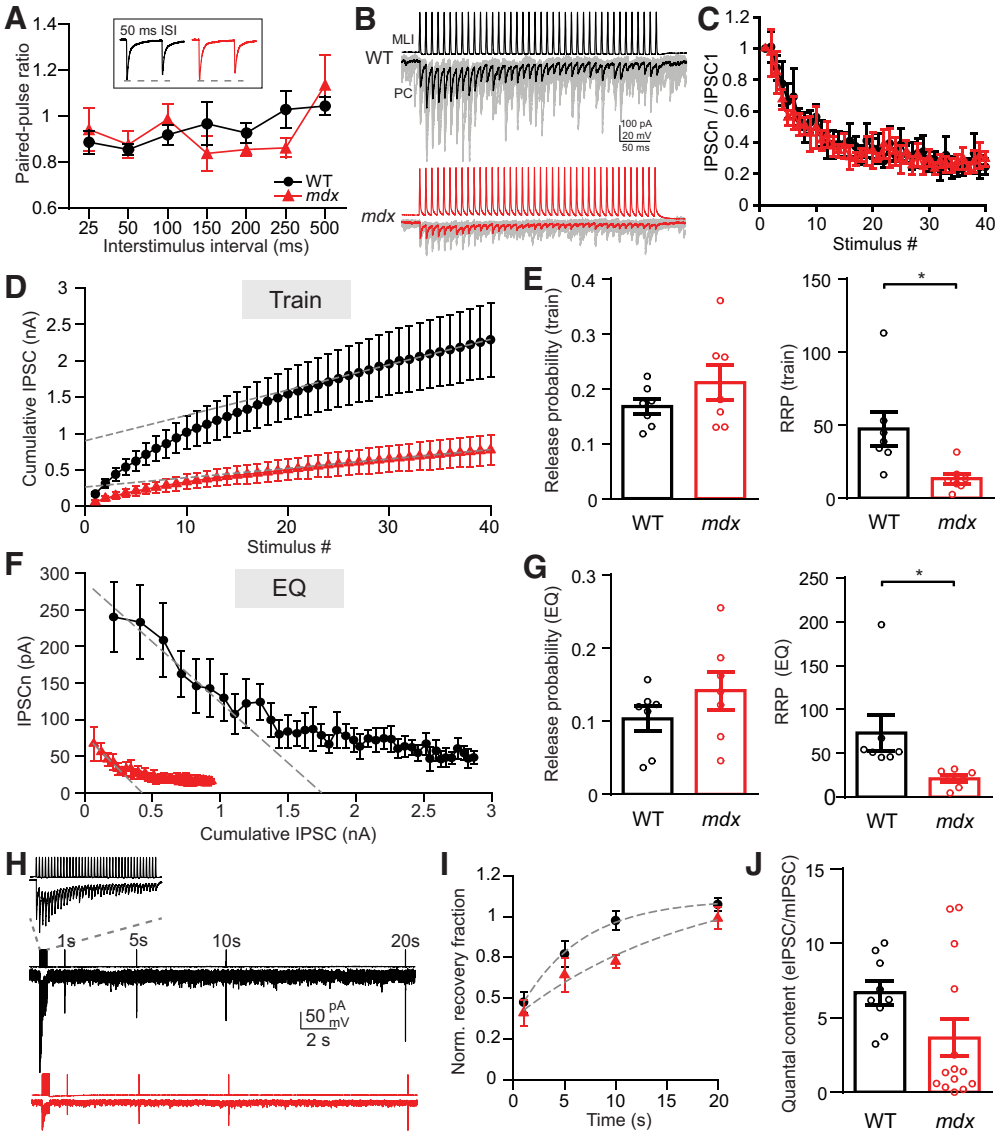

Figure 3. RRP, but not release probability, is reduced at MLI–PC synapses. ***A***, Average paired-pulse ratio ($IPSC_2/IPSC_1$) measured over a range of ISIs in WT (black) and mdx (red) PCs. Inset, Example traces showing pairs of IPSCs (50 ms ISI). ***B***, Representative traces of AP trains (100 Hz) in MLIs and evoked IPSCs (thin gray lines are individual sweeps, thick lines are average traces) in connected WT (black) and *mdx* (red) PCs. ***C***, Plots of IPSC amplitudes (normalized to the first IPSC) during a 100 Hz train of stimuli from WT (black) and *mdx* (red). The profiles of short-term plasticity and steady-state depression were not different between genotypes. ***D***, Average cumulative IPSC from WT (black) and *mdx* (red) MLI–PC synapses plotted against stimulus number. Linear fits to the last 15 points of each curve and the extrapolated *y*-intercept are also shown (gray dashed lines). ***E***, Average release probability (left) and readily releasable pool size (right) calculated from cumulative IPSC plots (train method). ***F***, Average IPSC amplitude from WT (black) and *mdx* (red) MLI–PC synapses plotted against cumulative IPSC amplitude. Linear fits to the first 5 points of each curve and extrapolated *x*-intercepts are also shown (gray dashed lines). ***G***, Average release probability (left) and readily releasable pool size (right) calculated from cumulative IPSC plots (EQ method). ***H***, Example traces of IPSC amplitude recovery following vesicle depletion in WT (black) and *mdx* (red) PCs. Inset, Expanded view of 100 Hz MLI AP train and resulting PC IPSCs used to deplete vesicles at MLI–PC synapses. ***I***, Plot of IPSC recovery over time (normalized to the first IPSC in the 100 Hz stimulus train) in WT (black) and *mdx* (red) PCs. Single exponential fits to recovery data points (gray dashed lines) are also shown. ***J***, Estimate of quantal content measured by dividing the first IPSC amplitude of each MLI–PC pair by the average mIPSC amplitude for each genotype. Circles in bar graphs represent individual data points. * $p < 0.05$.

PCs are almost entirely GABAergic, mainly arising from MLIs, with a small contribution from PC collateral axons (Altman, 1972; Ichikawa et al., 2011). We found that the total number of inhibitory synaptic densities contacting the PC soma was reduced in *mdx* PCs (WT: 5.39 ± 0.31, $n = 44$; *mdx*: 1.76 ± 0.23, $n = 37$; $p < 0.0001$; Fig. 5*C*). The perimeter of PCs was not different between genotypes ($p = 0.81$), and the reduction in inhibitory synapses persisted when normalized to PC perimeter (WT: 0.107 ± 0.007 AZ/μm, $n = 44$; *mdx*: 0.036 ± 0.005 AZ/μm, $n = 37$; $p < 0.0001$; Fig. 5*C*), suggesting that the difference in the number of synapses is not a product of differences in the size of the PC soma. Synapses arising from PC collateral axons were <3% of all inhibitory synapses counted, consistent with previous studies (Ichikawa et al., 2011) and were not different between genotypes ($p = 0.7$). We did not observe changes in general measures of PC soma morphology or stress (Table 1), suggesting that overall PC development and health are normal. We also found that the number of somatic spines decreased significantly from P16 to P19 (P16: 3.7 ± 0.7 spines/PC, $n = 10$; P19: 1.7 ± 0.4 spines/PC, $n = 10$; $p = 0.02$), as has been observed previously (Ichikawa et al., 2011). Spine number was not different between WT and *mdx* at either age ($p \geq 0.3$), suggesting that at least some aspects of synapse development proceed normally in *mdx* mice.

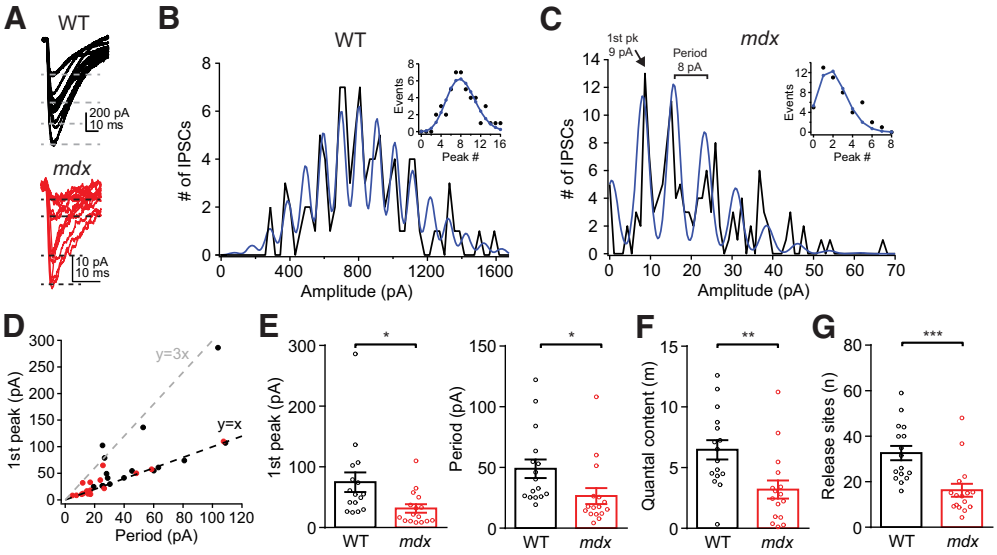

Figure 4. Quantal analysis of eIPSCs from MLI–PC pairs. ***A***, Examples of 15 consecutive eIPSC traces from WT (top) or *mdx* (bottom) MLI–PC paired recordings, showing quantal increases in IPSC amplitude. ***B***, ***C***, Frequency histogram of IPSC amplitudes and fit using the sum of Gaussian functions (blue) from WT (***B***) and *mdx* (***C***) PCs. Data from the same cells shown in ***A***. Inset, Histogram peaks (circles) and curve fit using a binomial function (blue line). ***D***, Plot showing correlation of the distance between histogram peaks (determined by the period of the Gaussian fitting function) and the value of the first histogram peak greater than zero for each MLI–PC pair. ***E***, Average amplitude of eIPSCs in the first histogram peak (left) and average period of Gaussian fit (right) in WT (black) and *mdx* (red) MLI–PC pairs. ***F***, ***G***, Average quantal content (m) of eIPSC and number of functional release sites (n) between WT (black) and *mdx* (red) MLI–PC pairs. Circles in bar graphs represent data from individual cells. * $p < 0.05$, ** $p < 0.01$, and *** $p < 0.001$.

In addition to the reduced number of synaptic contacts in *mdx* PCs, we also found changes in presynaptic morphology suggesting weaker synaptic connections. Specifically, the length of synaptic AZs was significantly reduced in *mdx* mice (WT: 297.2 ± 12.1 nm, $n = 110$; *mdx*: 239.3 ± 10.5 nm, $n = 72$; $p = 0.0009$; Fig. 5*D*). Also, the number of "docked" vesicles (vesicles within 10 nm of the AZ; WT: 1.95 ± 0.24 vesicles, $n = 38$; *mdx*: 1.32 ± 0.15 vesicles, $n = 37$; $p = 0.03$) or clustered vesicles (vesicles within 100 nm of AZ; WT: 7.6 ± 0.7 vesicles, $n = 38$; *mdx*: 4.9 ± 0.48 vesicles, $n = 37$; $p = 0.002$; vesicles within 200 nm of AZ; WT: 12.6 ± 1.1 vesicles, $n = 38$; *mdx*: 6.5 ± 0.7 vesicles, $n = 37$; $p < 0.00,001$; Fig. 5*E*) was reduced at inhibitory presynaptic terminals contacting *mdx* PCs. The difference in docked vesicle number disappeared when vesicle number was normalized to AZ length for each synapse (WT: 0.007 ± 0.001 vesicles/nm, $n = 38$; *mdx*: 0.006 ± 0.001 vesicles/nm, $n = 37$; $p = 0.2$), suggesting that the difference in docked vesicles may simply reflect shorter AZs in *mdx*. However, the reduction in clustered vesicles was maintained even when normalized to AZ length (within 200 nm of AZ; WT: 0.049 ± 0.003 vesicles/nm, $n = 38$; *mdx*: 0.028 ± 0.003 vesicles/nm, $n = 37$; $p < 0.00001$; Fig. 5*F*), suggesting that the loss of dystrophin may have additional effects on vesicle formation or translocation. These findings raise the possibility that the loss of postsynaptic dystrophin also produces changes in presynaptic structure and vesicle cycling. These data provide further anatomic evidence that dystrophin deficiency impairs the formation or maintenance of inhibitory synapses on PC bodies.

Dystrophin deficiency disrupts PC firing patterns

Next, we tested how dystrophin deficiency affects PCs on a functional level by measuring spontaneous AP firing (simple spikes) during cell-attached recordings in acute cerebellar slices (Fig. 6*A*). Somewhat surprisingly, reduced inhibition in *mdx* PCs did not correlate with increased average spontaneous firing rate (WT: 42.0 ± 1.5 Hz, $n = 48$; *mdx*: 42.8 ± 1.1 Hz, $n = 55$; $p = 0.67$; Fig. 6*A*,*B*), possibly the result of homeostatic mechanisms of PC firing (Smith and Otis, 2003; Achard and De Schutter, 2008). However, spontaneous firing in *mdx* PCs was significantly more regular compared with WT. This is evident by a reduction in the CV of ISIs (WT: 0.13 ± 0.01, $n = 48$; *mdx*: 0.095 ± 0.004, $n = 55$; $p = 0.003$; Fig. 6*C*) and a longer rightward tail in frequency distribution plots of WT ISIs (Fig. 6*A*, bottom). In whole-cell recordings, PC firing evoked from a hyperpolarized baseline by depolarizing steps (100 ms) was not different across genotypes (two-way repeated-measures ANOVA, $F_{(1,57)} = 0.34$; main effect, $p = 0.56$; Fig. 6*D*), suggesting that the intrinsic excitability of PCs is not changed. Measures of evoked AP waveform, including threshold, amplitude, maximum depolarizing slope, and afterhyperpolarization, were also not different across genotypes (Table 2). However, we did find a small, but significant, decrease in the AP half-width (WT: 0.25 ± 0.003 ms, $n = 30$; *mdx*: 0.22 ± 0.005 ms, $n = 29$; $p = 0.0004$) and an increase in maximum repolarizing slope during the falling phase of the AP (WT: 251.9 ± 7.3 mV/ms, $n = 30$; *mdx*: 290.8 ± 9.3 mV/ms, $n = 29$; $p = 0.0017$), possibly indicating a change in K^+ channel density or kinetics in *mdx* PCs. These data suggest that loss of dystrophin has little effect on intrinsic excitability or spontaneous firing in PCs, but the loss of inhibitory input allows for more regular pacemaker firing in these cells.

PCs are unusual because they fire APs spontaneously at high rates and an important downstream signal in the circuit may be a pause or reduction of firing. We therefore tested whether reduced synaptic inhibition in PCs would impair the ability of MLIs to pause PC firing. We made whole-cell recordings from MLIs and cell-attached recordings from connected PCs, allowing the PC to fire freely (Fig. 6*E*). We then tested the ability of trains of APs (100 ms at 50–250 Hz) evoked by current injections in the MLI to slow or pause PC firing. We found that in both genotypes, the inhibition of PC firing increased with increased MLI stimulation frequency. However, for each MLI firing frequency

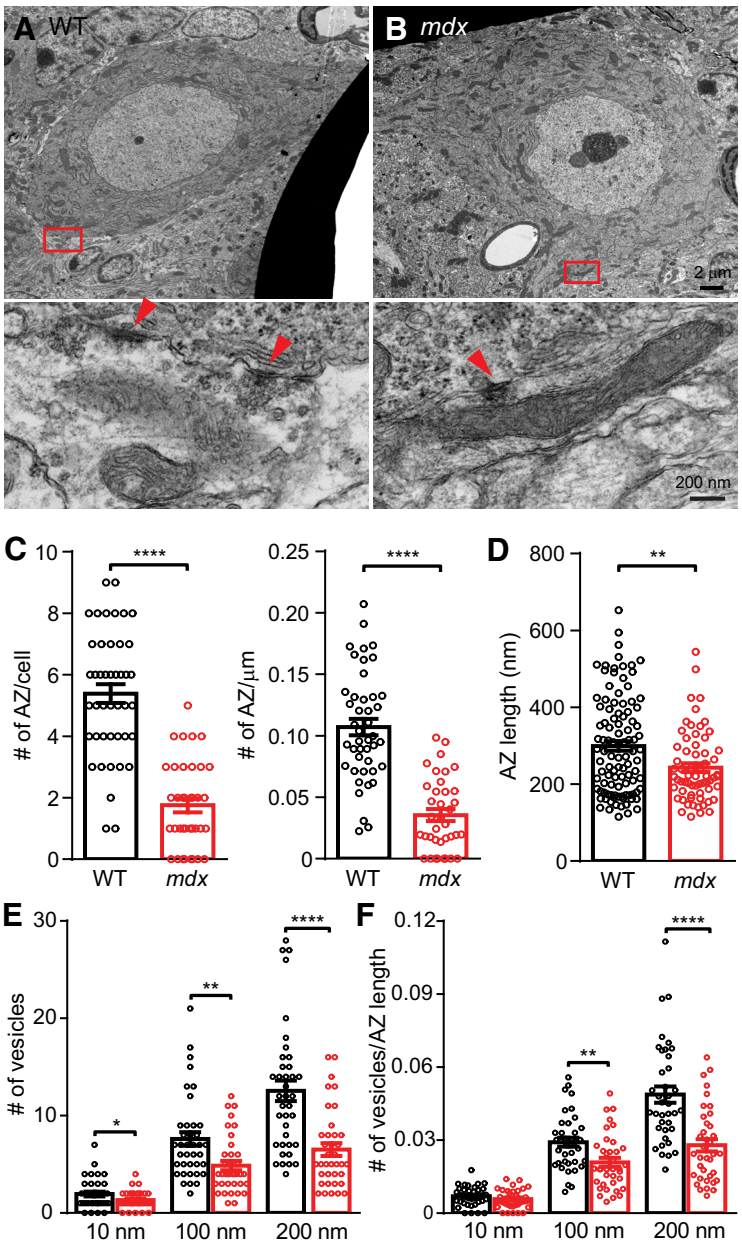

Figure 5. Reduced number of anatomically defined inhibitory synapses on *mdx* PC soma. ***A***, ***B***, Top, WT and *mdx* PC soma imaged at 4000×. Bottom, 50,000× magnification of the red boxes in the top panels. Red arrowheads indicate individual synaptic structures. ***C***, Average number of AZs per PC soma (left), and average number of AZs per micrometer of surface membrane (right). ***D***, Average AZ length. ***E***, Average number of synaptic vesicles within 10, 100, or 200 nm of the AZ in WT and *mdx*. ***F***, Average number of synaptic vesicles within 10, 100, or 200 nm of the AZ normalized to AZ length. Circles in bar graphs represent data from individual cells/synapses. * $p < 0.05$, ** $p < 0.01$, *** $p < 0.001$, and **** $p < 0.0001$.

Table 1. EM Analysis of PC morphology

	WT (*n*)	*mdx* (*n*)	*p* value
Nucleus perimeter (µm)	35.4 ± 1.0 (20)	36.4 ± 1.5 (17)	0.58
Nucleus area (µm^2)	82.3 ± 4.8 (20)	78.8 ± 6.4 (17)	0.66
Nucleus circularity	0.81 ± 0.02 (20)	0.72 ± 0.03 (17)	0.01
cDNA area (µm^2)	0.72 ± 0.14 (20)	1.33 ± 0.34 (17)	0.09
Nucleolus area (µm^2)	1.41 ± 0.48 (20)	2.50 ± 0.72 (17)	0.20
Mitochondria perimeter (µm)	4.60 ± 0.26 (39)	4.71 ± 0.30 (38)	0.30
Mitochondria circularity	0.54 ± 0.03 (39)	0.53 ± 0.03 (38)	0.27

Data presented as mean ± SEM with Student's *t* test. Measures of PC morphology and cellular stress, including the nucleus, cDNA, nucleolus, and mitochondria in WT and *mdx* PCs. *p* values comparing WT and *mdx* values for each measure are also listed.

there was less inhibition of PC firing in *mdx* compared with WT (two-way repeated-measures ANOVA, $F_{(1,16)}$=10.96; main effect, $p = 0.0044$; Fig. 6*F*). In *mdx* PCs, MLIs largely lost the ability to pause PC firing; even at high stimulation frequency, the PC firing rate was only mildly decreased (~20%). These data indicate that the loss of inhibitory synaptic transmission caused by dystrophin deficiency disrupts PC firing patterns and, potentially, downstream signaling in the cerebellar nuclei.

While acute brain slice recordings are valuable for elucidating the molecular and cellular mechanisms of dystrophin deficiency in PC function, it remains unclear as to how cerebellar circuit activity is disrupted by dystrophinopathy in the context of behavior. Therefore, we made *in vivo* extracellular electrophysiological recordings from PCs in awake WT and *mdx* mice using high-electrode density silicon probes (Fig. 7*A*). We found that the rate of spontaneous PC simple spike firing, measured while mice were in a state of resting quiescence, was not different across genotypes (WT: 68.5 ± 5.6 Hz, $n = 25$; *mdx*: 66.6 ± 5.0 Hz, $n = 22$; Mann–Whitney test, $p = 0.9$; Fig. 7*B*), consistent with our findings in acute slices (Fig. 6*B*). However, unlike our slice recordings, we did not observe a significant change in the regularity of spontaneous AP firing (ISI CV: WT: 0.74 ± 0.07, $n = 25$; *mdx*: 0.68 ± 0.04, $n = 22$; Mann–Whitney test, $p = 0.71$; Fig. 7*C*). Overall, PC simple spike firing *in vivo* was significantly more irregular compared with slice recordings ($p < 0.0001$), likely because of the engagement of additional circuit elements missing in the slice preparation. The greater irregularity of spontaneous firing *in vivo* likely masks the comparatively subtle change in regularity that we observed in the slice preparation.

We also measured the modulation of PC firing in response to an unexpected sensory stimulus (250 ms tone or light flash). We found approximately equal numbers of PCs with positively modulating (Fig. 7*D*) and negatively modulating (Fig. 7*G*) simple spike firing patterns during the sensory stimulus in both WT and *mdx* mice. In positively modulating PCs, we found that the mean percentage change in firing was not significantly different between genotypes (WT: 16.6 ± 2.6%, $n = 13$; *mdx*: 28.1 ± 6.2%, $n = 13$; Mann–Whitney test, $p = 0.09$; Fig. 7*E*), but the peak percentage change in firing rate was greater in *mdx* mice (WT: 64.7 ± 9.9%; *mdx*: 110.2 ± 10.8%; Mann–Whitney test, $p = 0.0005$; Fig. 7*F*), which is consistent with reduced MLI-mediated feedforward inhibition. Surprisingly, we did not observe a difference in the mean percentage change (WT: 8.4 ± 0.9%, $n = 12$; *mdx*: 10.4 ± 1.1%, $n = 10$; Mann–Whitney test, $p = 0.12$; Fig. 7*H*) or

peak percentage change (WT: 63.7 ± 4.0%; *mdx*: 63.4 ± 10.9%; Mann–Whitney test, $p = 0.99$; Fig. 7*I*) of firing rate in negatively modulating PCs. Together, these data suggest that reduced inhibition in *mdx* PCs has little effect on baseline simple spike firing *in vivo* but allows for greater positive modulation of firing during sensory stimulation, possibly affecting synaptic plasticity and downstream signaling at PC targets in the cerebellar nuclei.

Discussion

Pathophysiology of central neuronal circuits is an important, but poorly understood, aspect of DMD. We found that loss of dystrophin in PCs reduces inhibitory synaptic function by at least two mechanisms. Using analysis of mIPSCs and quantal analysis of eIPSCs, we show that the quantal amplitude of inhibitory responses is reduced in *mdx* PCs, which is consistent with previous reports showing reduced $GABA_AR$ clustering (Knuesel et al., 1999; Grady et al., 2006). However, our electrophysiology and EM results also demonstrate a reduction in the number of inhibitory synapses contacting each PC. These data raise the possibility that dystrophin (and the DGC protein complex) acts as a cell adhesion molecule at inhibitory synapses in addition to, or instead of, a receptor clustering molecule. Furthermore, recordings from *mdx* cerebellar slices showed impaired MLI-mediated pausing of PC firing and *in vivo* recordings from awake *mdx* mice revealed greater sensory-evoked firing in positively modulating PCs. These data reveal potentially novel functions of dystrophin in the CNS, which may explain the high comorbidity with neurodevelopmental (Wu et al., 2005; Pane et al., 2012; Fujino et al., 2018) and cognitive (Hinton et al., 2000; Cotton et al., 2005) disorders observed in DMD.

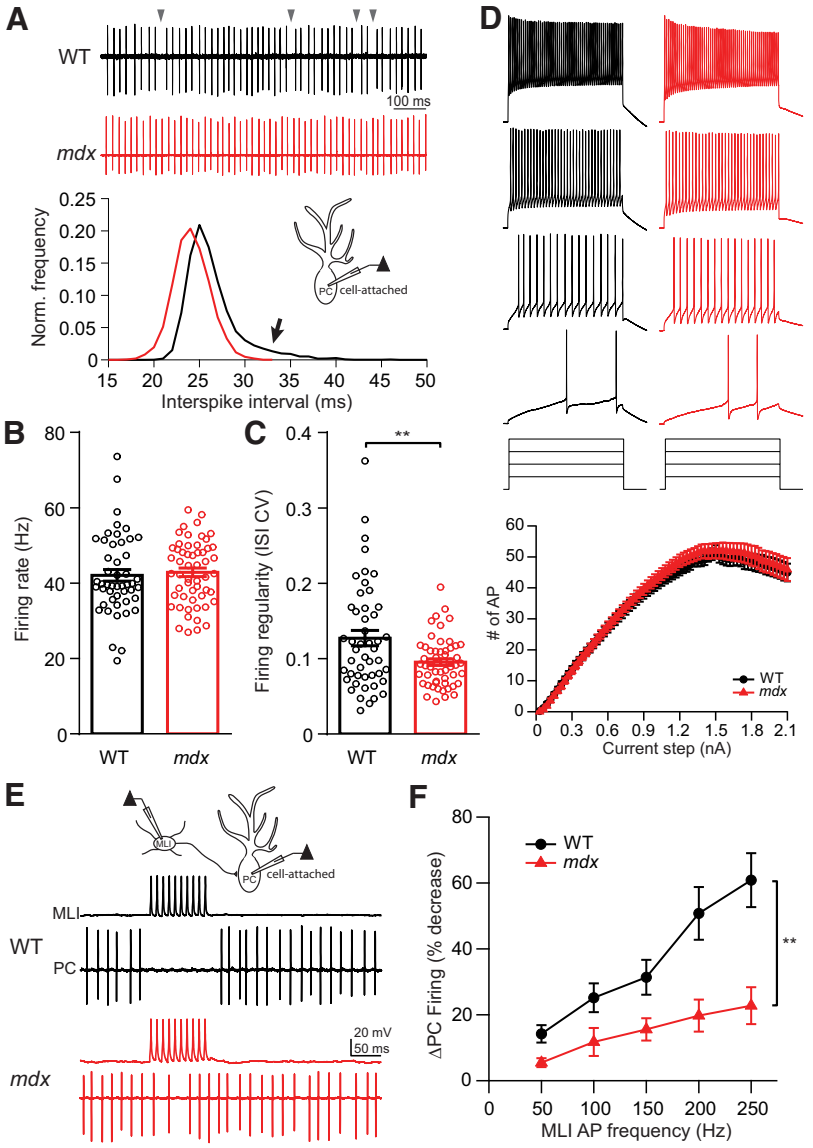

Figure 6. *Ex vivo* slice measurement of PC activity. ***A***, Top, Representative cell-attached traces of spontaneous firing from a WT (black) and *mdx* (red) PC. Gray arrowheads indicate prolonged ISIs in WT PC. Bottom, Representative normalized frequency distribution of ISIs recorded from a WT (black) and an *mdx* (red) PC. Arrow indicates larger rightward tail of the distribution in the WT cell. ***B***, Average PC spontaneous firing rate. ***C***, Average CV of ISIs. ***D***, Representative traces of PC firing during step current injections as a measure of intrinsic excitability and average input–output curves resulting from step current injections (bottom). ***E***, Diagram of MLI–PC paired recording configuration (top) and representative traces of simultaneously recorded APs evoked in an MLI and spontaneous firing from a WT (black) and *mdx* (red) PC, showing MLI-mediated pause/reduction in PC firing. ***F***, Average change in PC firing rate during stimulation of APs in a connected MLI over a range of frequencies (50–250 Hz). Circles in bar graphs represent individual data points. ** $p < 0.01$.

Several lines of evidence suggest that dystrophin is required for proper $GABA_AR$ clustering in PCs. Dystrophin colocalizes with postsynaptic $GABA_AR$ clusters, and the loss of dystrophin results in a reduced number and size of receptor clusters in *mdx* PCs (Knuesel et al., 1999; Grady et al., 2006). However, a recent study saw no change in $GABA_AR$ ($\alpha 1$ or $\gamma 2$), neuroligin2, or gephyrin labeling at PC inhibitory synapses in *mdx* mice, calling into question whether dystrophin is necessary for the organization of postsynaptic densities or receptor clustering (Briatore et al., 2020). Other studies have observed reduced mIPSC amplitude and frequency in *mdx* PCs, attributing these changes to reduced $GABA_AR$ clustering (Anderson et al., 2003; Kueh et al., 2008, 2011). Our data suggest that the loss of inhibitory vesicle release sites plays an equal or larger role in reducing inhibition. In recordings from connected MLI–PC pairs, we found that IPSCs evoked by single MLI APs were reduced by ~60%. This reduction could result from reduced release probability, a reduced number of synapses/release sites, or reduced clustering of $GABA_ARs$. We found no change in release probability, measured by PPR or analysis of cumulative IPSCs. We estimate that reduced $GABA_AR$ clustering accounts for 25–40% reduction in eIPSC amplitude based on changes in mIPSC amplitude and the quantal response amplitude obtained from quantal analysis. However, measurements of the RRP size, number of functional release sites, and number of AZs from EM images are consistently reduced in *mdx* PCs by 50–65%. Based on these findings, we propose that loss of inhibitory synaptic connections accounts for a larger portion of the reduced IPSCs

Table 2. Purkinje cell action potential waveform analysis

	AP amplitude (mV)	Threshold (mV)	Half-width (ms)	Dep. slope (mV/ms)	Rep. slope (mV/ms)	AHP amplitude (mV)
WT, $n = 30$ (5)	51.8 ± 1.1	−47.5 ± 0.8	0.25 ± 0.003	326.3 ± 7.4	−251.9 ± 7.3	10.5 ± 0.5
mdx, $n = 29$ (7)	52.5 ± 0.7	−47.9 ± 0.8	0.22 ± 0.005	336.8 ± 8.2	−290.8 ± 9.3	10.3 ± 0.6
p value	0.58	0.70	0.0004	0.35	0.002	0.85

Data are presented as the mean ± SEM with Student's t test. Measurements of PC AP waveform. Measures of evoked AP waveform, including AP amplitude, threshold, half-width, maximum depolarizing slope (Dep. slope), maximum repolarizing slope (Rep. slope), and amplitude of the afterhyperpolarization (AHP) from WT and *mdx* PCs. p Values comparing WT and *mdx* values for each measure are also listed.

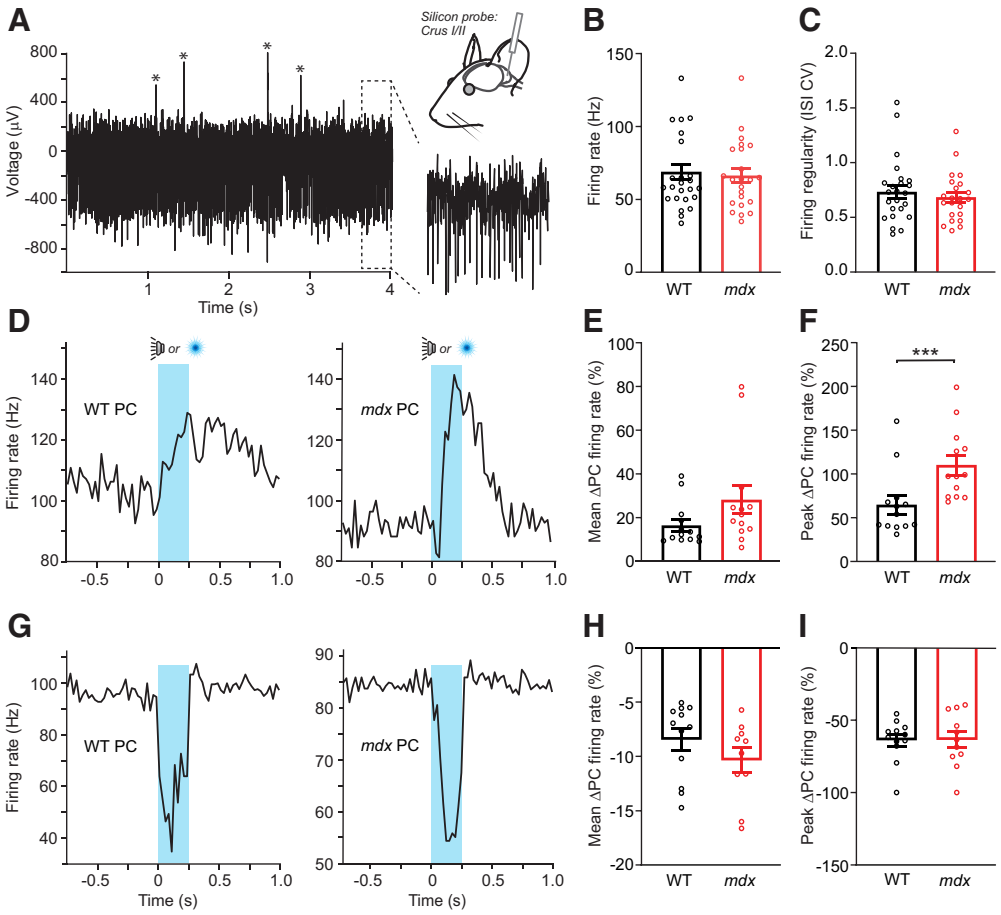

Figure 7. *In vivo* measurement of PC activity. ***A***, Extracellular unit recordings were obtained from PCs located in left lobules Crus I or Crus II from WT ($n = 5$) or *mdx* ($n = 4$) mice. The voltage trace from an example PC shows abundant simple spikes that are clearly apparent in the expanded view as well as complex spikes (marked by asterisks). ***B***, ***C***, Across-genotype comparison of mean simple spike firing rate and variability of PCs during quiescence. ***D***, Average peristimulus time histograms for two positively modulating PCs in response to trials of unexpected sensory stimuli (the timing of audible tones or light flashes is indicated in blue). ***E***, ***F***, Although there was no difference in the mean firing rate of sensory-evoked simple spiking between genotypes ($p = 0.09$), there was a significant increase in the peak firing rate of positively modulating PCs from *mdx* mice relative to WTs ($p = 0.0005$). ***G***, Average peristimulus time histograms for two negatively modulating PCs. ***H***, ***I***, Across-genotype comparison of the mean and the peak rate of diminished simple spike firing for negatively modulating PCs during unexpected sensory stimuli. *** $p < 0.001$.

compared with reduced postsynaptic receptor clustering, which is consistent with recent findings in PCs lacking β-dystroglycan expression (another component of the DGC; Briatore et al., 2020).

Our finding that RRP size, the number of functional release sites, and the number of anatomic AZs are all reduced by ~60% in *mdx* PCs suggests that dystrophin may play a role in synapse formation or maintenance in PCs. Dystrophin is a member of the larger DGC, which spans the cell membrane. In muscle cells, the DGC is anchored to the intracellular actin cytoskeleton by dystrophin and binds to extracellular matrix proteins, including laminins, through α-dystroglycan (Gao and McNally, 2015). In neuronal cells, dystrophin also anchors the DGC to actin, but extracellular binding partners of the DGC are unclear (Grady et al., 2006; Briatore et al., 2020). At least one investigation found that α-dystroglycan binds tightly to neurexin LNS (laminin neurexin sex hormone binding protein) domains, a presynaptic cell adhesion protein (Sugita et al., 2001), raising the possibility that the DGC acts as a synaptic adhesion molecule. Interestingly, neuroligin triple-knock-out mice (a neurexin binding partner) display a similar phenotype at inhibitory synapses in PCs, with substantially reduced IPSC amplitude and mIPSC frequency, and little or no change in IPSC kinetics and PPR (Zhang et al., 2015). Neurexin mutations are highly associated with development of autism spectrum disorder (Tromp et al., 2021). Direct binding between neurexins and DGC at inhibitory synapses may, at least in part, explain the high comorbidity between DMD and autism.

Our data indicate that inhibitory synaptic contacts are reduced in *mdx* PCs. However, it is not clear whether this results

from the failure of synapses to form during early development or increased postnatal loss of synapses. Data showing detailed developmental expression of dystrophin in the mouse cerebellum are not currently available. Previous work shows that dystrophin (Dp427) or other components of the DGC are expressed during early prenatal development in the human and mouse cerebellum, respectively (Holder et al., 1996; Janke et al., 2013; Doorenweerd et al., 2017), which is consistent with dystrophin and the DGC participating in synapse formation. However, additional experiments using tamoxifen-inducible dystrophin knock-out mice or dystrophin rescue in postnatal *mdx* mice will be necessary to determine the precise role of dystrophin in synapse formation and maintenance.

Dysfunction of the cerebellar circuit has been hypothesized to contribute to cognitive and motor phenotypes associated with DMD (Marini et al., 2007; Cyrulnik and Hinton, 2008). However, physiological changes in cerebellar signaling following the loss of dystrophin are still poorly understood. In acute slice recordings, we found that spontaneous firing in PCs is more regular in *mdx* mice. We attribute this change primarily to the loss of inhibitory synaptic currents that can prolong ISIs when present, which is in agreement with a previous study demonstrating more regular firing in PCs following pharmacological blockade of $GABA_A$Rs (Häusser and Clark, 1997). It is also possible that larger or faster K^+ currents, indicated by reduced AP half-width and faster repolarization, may contribute to more regular firing in *mdx* mice (Walter et al., 2006). However, *in vivo* recordings of PC firing did not show a change in simple spike firing regularity (Fig. 7*C*), which is consistent with previous findings in *mdx* mice (Stay et al., 2019). Overall, firing is significantly more irregular *in vivo* (CV, ~0.7 vs ~0.1; Figs. 6*C*, 7*C*; Stay et al., 2019), likely because of the presence of complex spikes or other mechanism of firing variability not present in the slice preparation, which masks the relatively small change in regularity observed in slices. We did not observe a change in the simple spike firing rate in slices or *in vivo* recordings (Figs. 6*B*, 7*B*). In contrast, Stay et al. (2019) found decreased PC firing rate in awake female *mdx* mice. This discrepancy may result from sex differences in *mdx* mice (the present study used male mice) or recording location (PC recordings from Stay et al., 2019, were relatively medial to those presented here), which will need to be explored further.

While the rate and regularity of spontaneous PC firing may influence cerebellar function (Walter et al., 2006; Person and Raman, 2011), dynamic modulation of PC firing likely has a larger effect on cerebellar behavior and learning. Because PCs spontaneously fire simple spikes at high rates, synaptic input can drive either elevated or reduced firing. We found that the peak firing rate of positively modulating PCs by sensory stimulation was increased in *mdx* mice (Fig. 7*F*), which is consistent with reduced feedforward inhibition. Because PCs inhibit their downstream target neurons in the cerebellar nuclei (which also fire spontaneously), this change is expected to produce a larger pause or reduction in firing in these neurons, altering synaptic plasticity in the cerebellar nuclei (Zhang et al., 2004; Pugh and Raman, 2006) and the output of the cerebellar circuit. We did not observe a change in sensory-evoked firing from negatively modulating PCs in *mdx* mice. This result is surprising because (1) negative modulation of PC firing is almost certainly mediated by inhibition from MLIs, which all other evidence suggests is reduced in *mdx* mice; and (2) negative modulation of PC firing was reduced in paired MLI–PC recordings in slices. This result may be explained by a shift in the balance of synaptic and extrasynaptic $GABA_A$Rs in *mdx* PCs. Our data and previous studies show that synaptic clustering of $GABA_A$Rs is reduced in *mdx* PCs (Knuesel et al., 1999; Grady et al., 2006), raising the possibility that extrasynaptic $GABA_A$Rs are increased in these cells. If this is the case, stimuli that selectively activate synaptic $GABA_A$Rs, such as low levels of MLI input (as is expected at PCs with positive modulation of firing) or stimulation of a single MLI in slices, would likely result in reduced inhibition. However, stimuli that elicit high-frequency activity from multiple MLIs, as is likely onto PCs that negatively modulate their firing, may produce extensive spillover and pooling of GABA in the extrasynaptic space (Mitchell and Silver, 2000; Pugh and Jahr, 2011). In this case, a greater density of extrasynaptic $GABA_A$Rs in *mdx* PCs may produce a net inhibitory current similar to that experienced by WT PCs, despite reduced synaptic $GABA_A$R currents. Together, these data suggest that the loss of dystrophin disrupts PC firing patterns *in vivo*, but the level of disruption may depend on the degree of MLI activation, which must be explored in future experiments.

References

Achard P, De Schutter E (2008) Calcium, synaptic plasticity and intrinsic homeostasis in Purkinje neuron models. Front Comput Neurosci 2:8.

Altman J (1972) Postnatal development of the cerebellar cortex in the rat. II. Phases in the maturation of Purkinje cells and of the molecular layer. J Comp Neurol 145:399–464.

Anderson JL, Head SI, Morley JW (2003) Altered inhibitory input to Purkinje cells of dystrophin-deficient mice. Brain Res 982:280–283.

Billard C, Gillet P, Signoret JL, Uicaut E, Bertrand P, Fardeau M, Barthez-Carpentier MA, Santini JJ (1992) Cognitive functions in Duchenne muscular dystrophy: a reappraisal and comparison with spinal muscular atrophy. Neuromuscul Disord 2:371–378.

Boyd IA, Martin AR (1956) The end-plate potential in mammalian muscle. J Physiol 132:74–91.

Briatore F, Pregno G, Di Angelantonio S, Frola E, De Stefano ME, Vaillend C, Sassoè-Pognetto M, Patrizi A (2020) Dystroglycan mediates clustering of essential GABAergic components in cerebellar Purkinje cells. Front Mol Neurosci 13:164.

Castellucci VF, Kandel ER (1974) A quantal analysis of the synaptic depression underlying habituation of the gill-withdrawal reflex in Aplysia. Proc Natl Acad Sci U S A 71:5004–5008.

Cotton S, Voudouris NJ, Greenwood KM (2001) Intelligence and Duchenne muscular dystrophy: full-scale, verbal, and performance intelligence quotients. Dev Med Child Neurol 43:497–501.

Cotton SM, Voudouris NJ, Greenwood KM (2005) Association between intellectual functioning and age in children and young adults with Duchenne muscular dystrophy: further results from a meta-analysis. Dev Med Child Neurol 47:257–265.

Cyrulnik SE, Hinton VJ (2008) Duchenne muscular dystrophy: a cerebellar disorder? Neurosci Biobehav Rev 32:486–496.

Darmahkasih AJ, Rybalsky I, Tian C, Shellenbarger KC, Horn PS, Lambert JT, Wong BL (2020) Neurodevelopmental, behavioral, and emotional symptoms common in Duchenne muscular dystrophy. Muscle Nerve 61:466–474.

Doorenweerd N, Mahfouz A, van Putten M, Kaliyaperumal R, T' Hoen PAC, Hendriksen JGM, Aartsma-Rus AM, Verschuuren JJGM, Niks EH, Reinders MJT, Kan HE, Lelieveldt BPF (2017) Timing and localization of human dystrophin isoform expression provide insights into the cognitive phenotype of Duchenne muscular dystrophy. Sci Rep 7:12575.

Duchenne G (1868) Recherches sur la paralysie musculaire pseudo-hypertrophique, ou paralysie myo-sclerosique. Arch Gen Med 11:5–25.

Edwards FA, Konnerth A, Sakmann B (1990) Quantal analysis of inhibitory synaptic transmission in the dentate gyrus of rat hippocampal slices: a patch-clamp study. J Physiol 430:213–249.

Elmqvist D, Quastel DM (1965) A quantitative study of end-plate potentials in isolated human muscle. J Physiol 178:505–529.

Emery AEH (1991) Population frequencies of inherited neuromuscular diseases—a world survey. Neuromuscul Disord 1:19–29.

Fujino H, Saito T, Matsumura T, Shibata S, Iwata Y, Fujimura H, Imura O (2018) Autism spectrum disorders are prevalent among patients with dystrophinopathies. Neurol Sci 39:1279–1282.

Gaffield MA, Christie JM (2021) The cerebellum encodes and influences the initiation and termination of discontinuous movements. bioRxiv.

Gao Q, McNally EM (2015) The dystrophin complex: structure, function and implications for therapy. Compr Physiol 5:1223–1239.

Geng Y, Sicinski P, Gorecki D, Barnard PJ (1991) Developmental and tissue-specific regulation of mouse dystrophin: the embryonic isoform in muscular dystrophy. Neuromuscul Disord 1:125–133.

Grady RM, Wozniak DF, Ohlemiller KK, Sanes JR (2006) Cerebellar synaptic defects and abnormal motor behavior in mice lacking α- and β-dystrobrevin. J Neurosci 26:2841–2851.

Häusser M, Clark BA (1997) Tonic synaptic inhibition modulates neuronal output pattern and spatiotemporal synaptic integration. Neuron 19:665–678.

Hinton VJ, De Vivo DC, Nereo NE, Goldstein E, Stern Y (2000) Poor verbal working memory across intellectual level in boys with Duchenne dystrophy. Neurology 54:2127–2132.

Holder E, Maeda M, Bies RD (1996) Expression and regulation of the dystrophin Purkinje promoter in human skeletal muscle, heart, and brain. Hum Genet 97:232–239.

Ichikawa R, Yamasaki M, Miyazaki T, Konno K, Hashimoto K, Tatsumi H, Inoue Y, Kano M, Watanabe M (2011) Developmental switching of perisomatic innervation from climbing fibers to basket cell fibers in cerebellar Purkinje cells. J Neurosci 31:16916–16927.

Janke A, Upadhaya R, Snow WM, Anderson JE (2013) A new look at cytoskeletal NOS-1 and β-dystroglycan changes in developing muscle and brain in control and mdx dystrophic mice. Dev Dyn 242:1369–1381.

Karagan NJ, Richman LC, Sorensen JP (1980) Analysis of verbal disability in Duchenne muscular dystrophy. J Nerv Ment Dis 168:419–423.

Khatri SN, Wu WC, Yang Y, Pugh JR (2019) Direction of action of presynaptic GABAA receptors is highly dependent on the level of receptor activation. J Neurophysiol 121:1896–1905.

Knuesel I, Mastrocola M, Zuellig RA, Bornhauser B, Schaub MC, Fritschy JM (1999) Short communication: altered synaptic clustering of GABAA receptors in mice lacking dystrophin (mdx mice). Eur J Neurosci 11:4457–4462.

Kueh SL, Head SI, Morley JW (2008) GABA(A) receptor expression and inhibitory post-synaptic currents in cerebellar Purkinje cells in dystrophin-deficient mdx mice. Clin Exp Pharmacol Physiol 35:207–210.

Kueh SL, Dempster J, Head SI, Morley JW (2011) Reduced postsynaptic GABAA receptor number and enhanced gaboxadol induced change in holding currents in Purkinje cells of the dystrophin-deficient mdx mouse. Neurobiol Dis 43:558–564.

Lidov HG, Byers TJ, Kunkel LM (1993) The distribution of dystrophin in the murine central nervous system: an immunocytochemical study. Neuroscience 54:167–187.

Marini A, Lorusso ML, D'Angelo MG, Civati F, Turconi AC, Fabbro F, Bresolin N (2007) Evaluation of narrative abilities in patients suffering from Duchenne muscular dystrophy. Brain Lang 102:1–12.

Martin AR (1966) Quantal nature of synaptic transmission. Physiol Rev 46:51–66.

Massopust RT, Lee YI, Pritchard AL, Nguyen VM, McCreedy DA, Thompson WJ (2020) Lifetime analysis of mdx skeletal muscle reveals a progressive pathology that leads to myofiber loss. Sci Rep 10:17248.

Mitchell SJ, Silver RA (2000) Glutamate spillover suppresses inhibition by activating presynaptic mGluRs. Nature 404:498–502.

Muntoni F, Mateddu A, Marchei F, Clerk A, Serra G (1993) Muscular weakness in the mdx mouse. J Neurol Sci 120:71–77.

Pachitariu M, Steinmetz N, Kadir S, Carandini M, Harris KD (2016) Kilosort: realtime spike-sorting for extracellular electrophysiology with hundreds of channels. bioRxiv. doi: 10.1101/061481.

Palay SL, Chan-Palay V (1974) Cerebellar cortex, cytology and organization. Berlin: Springer.

Pane M, Lombardo ME, Alfieri P, D'Amico A, Bianco F, Vasco G, Piccini G, Mallardi M, Romeo DM, Ricotti V, Ferlini A, Gualandi F, Vicari S, Bertini E, Berardinelli A, Mercuri E (2012) Attention deficit hyperactivity disorder and cognitive function in Duchenne muscular dystrophy: phenotype genotype correlation. J Pediatr 161:705–709.

Person AL, Raman IM (2011) Purkinje neuron synchrony elicits time-locked spiking in the cerebellar nuclei. Nature 481:502–505.

Pugh JR, Jahr CE (2011) Axonal $GABA_A$ receptors increase cerebellar granule cell excitability and synaptic activity. J Neurosci 31:565–574.

Pugh JR, Raman IM (2006) Potentiation of mossy fiber EPSCs in the cerebellar nuclei by NMDA receptor activation followed by postinhibitory rebound current. Neuron 51:113–123.

Ricotti V, Mandy WP, Scoto M, Pane M, Deconinck N, Messina S, Mercuri E, Skuse DH, Muntoni F (2016) Neurodevelopmental, emotional, and behavioural problems in Duchenne muscular dystrophy in relation to underlying dystrophin gene mutations. Dev Med Child Neurol 58:77–84.

Sabatini BL, Regehr WG (1999) Timing of synaptic transmission. Annu Rev Physiol 61:521–542.

Schneggenburger R, Meyer AC, Neher E (1999) Released fraction and total size of a pool of immediately available transmitter quanta at a calyx synapse. Neuron 23:399–409.

Smith SL, Otis TS (2003) Persistent changes in spontaneous firing of Purkinje neurons triggered by the nitric oxide signaling cascade. J Neurosci 23:367–372.

Stay TL, Miterko LN, Arancillo M, Lin T, Sillitoe RV (2019) In vivo cerebellar circuit function is disrupted in an mdx mouse model of Duchenne muscular dystrophy. Dis Model Mech 13:dmm040840.

Stell BM, Rostaing P, Triller A, Marty A (2007) Activation of presynaptic $GABA_A$ receptors induces glutamate release from parallel fiber synapses. J Neurosci 27:9022–9031.

Sugita S, Saito F, Tang J, Satz J, Campbell K, Südhof TC (2001) A stoichiometric complex of neurexins and dystroglycan in brain. J Cell Biol 154:435–445.

Takahashi KA, Linden DJ (2000) Cannabinoid receptor modulation of synapses received by cerebellar Purkinje cells. J Neurophysiol 83:1167–1180

Thanawala MS, Regehr WG (2013) Presynaptic calcium influx controls neurotransmitter release in part by regulating the effective size of the readily releasable pool. J Neurosci 33:4625–4633.

Tromp A, Mowry B, Giacomotto J (2021) Neurexins in autism and schizophrenia-a review of patient mutations, mouse models and potential future directions. Mol Psychiatry 26:747–760.

Walter JT, Alviña K, Womack MD, Chevez C, Khodakhah K (2006) Decreases in the precision of Purkinje cell pacemaking cause cerebellar dysfunction and ataxia. Nat Neurosci 9:389–397.

Wu JY, Kuban KC, Allred E, Shapiro F, Darras BT (2005) Association of Duchenne muscular dystrophy with autism spectrum disorder. J Child Neurol 20:790–795.

Zhang B, Chen LY, Liu X, Maxeiner S, Lee SJ, Gokce O, Südhof TC (2015) Neuroligins sculpt cerebellar Purkinje-cell circuits by differential control of distinct classes of synapses. Neuron 87:781–796.

Zhang W, Shin JH, Linden DJ (2004) Persistent changes in the intrinsic excitability of rat deep cerebellar nuclear neurones induced by EPSP or IPSP bursts. J Physiol 561:703–719.